



Baseline-Free Damage Identification in Plate Containing a Circular Hole with Edge Cracks Based on Lamb Wave Scattering

Mohammadreza Jalalinia¹ · Gholamreza Ghodrati Amiri¹ · Seyed Ali Seyed Razzaghi²

Received: 14 July 2021 / Revised: 2 May 2022 / Accepted: 29 June 2022 / Published online: 2 August 2022
© Krishtel eMaging Solutions Private Limited 2022

Abstract

Purpose Most Lamb wave-based damage detection techniques use scattering signals obtained from the subtraction of baseline and current signals. This article presents a baseline-free damage detection method based on the signals scattered by the damage in plate-like structures containing a circular hole with edge cracks using guided ultrasonic waves (GUWs) and signal processing.

Methods First, the GUWs were generated by simulating 16 transducers, using finite element analysis and ABAQUS. The location of transducers on the plate were set in a way that similar paths were made for waves traveling from actuators to sensors. Then, the differences between the similar path signals (residual signals) were obtained. The damaged path and arrival time of the scattered wave from the defect to the sensor location were determined using the wavelet coefficients obtained from continuous wavelet transform of the residual signals. Finally, to identify damage locations, arrival time data is applied in a probabilistic approach.

Results and Conclusion The numerical simulation results reveal that the baseline-free approach is able to accurately detect the location of the multiple damages occurred at the hole edge. Further, in order to investigate the effect of the edges of the plate on the results of damage detection, the transducers were considered at different distances from the edge of the hole. By ignoring the damage index values obtained at the edges of the plate, it can be stated that even when the transducers are located near the edges of the plate, the proposed method can detect the crack location at the edge of the hole.

Keywords Baseline-free · Damage detection · Wave propagation · Continuous wavelet transform · Plate with hole · Finite element simulation

Introduction

Today, nondestructive evaluation and structural health monitoring (SHM), in space, marine, and civil industries have been developed to reduce the maintenance costs and prevent sudden failures. Guided ultrasonic waves (GUWs) are widely recognized as an effective tool for non-destructive evaluation and SHM of structural components [1, 2]. The GUWs can propagate at long distances with little amplitude loss, and thus can provide cost-effective monitoring techniques [3]. From a single sensor location, they

can cover large areas, which helps to reduce the cost and time of inspection. However, the propagation of GUWs is strongly influenced by the parameters such as the frequency of excitation, the thickness of the structure, the material properties, direction of propagation and inter-laminar conditions which complicate the analysis of these waves [4]. Lamb waves are a type of GUWs in which waves travel within a thin plate (relative to propagating wavelength), they cause out-of-plane (i.e. perpendicular to the surfaces of the plate) and in-plane (i.e. parallel to their propagation direction) vibrations. These waves are the most commonly used GUWs in damage detection using pulse-echo [5], pitch-catch [6], and time-reversal (TR) [7] techniques. Masurkar and Yelve [8] performed experiments, wherein they used Lamb waves to find the location of damage as a small enclosed area formed by the intersection of various curves generated by the Asteroid algorithm. They used the Euclidean and Lagrange

✉ Gholamreza Ghodrati Amiri
ghodrati@iust.ac.ir

¹ School of Civil Engineering, Iran University of Science and Technology, Narmak, PO BOX 16765-163, Tehran, Iran

² Department of Civil Engineering, Payame Noor University, Tehran, Iran

optimization methods in order to further refine the damage location in the enclosed area. An experimental study of a baseline-free damage detection technique using time reversibility of Lamb wave for a woven-fabric composite laminate presented by Poddar et al. [9].

The GUWs, due to the sensitivity and high versatility, have a tremendous potential to identify imperfections. However, there are complexities in the interpretation of wave data and the precise description of the specifications [10]. In each guided wave excitation, often multiple modes are created [11]. The resulted wave signals are in a complex wave form due to the presence of unwanted modes. Therefore, it is challenging to identify important parameters that describe the defect profile, such as peak amplitude, peak location and the arriving time of each mode.

Signal processing methods have been adopted to reduce the complexity of registered wave signals. A major objective of any GUW-based SHM is to extract damage sensitive properties which indicate the existence, location and severity of the damage. Recently, several signal processing tools, such as discrete wavelet transform (DWT) [12, 13] and continuous wavelet transform (CWT) [14, 15] are applied to extract features sensitive to damage. These transforms can be used for damage detection and localization. Su et al. [16] proposed an identification approach for delamination locating in laminated composites based on the Lamb wave propagation. They used CWT and DWT for the signal processing to effectively diminish the influence of broadband noises. Yelve et al. [17] presented two algorithms namely curve-intersection and sub-quadrant algorithms for finding location of a damage in a planar structure. They calculated the arrival time data (time from the actuator to the damage and then from damage to the sensor) by processing the residual signal using CWT, which is further used in the proposed algorithms to find the location of a damage. Wang et al. [18] developed an algorithm based on correlation analysis to estimate the probability of the presence of damage in aluminum plates using Lamb wave signals from an active sensor network. They used the Shannon entropy optimization criterion to calibrate the optimal mother wavelet and the most appropriate continuous wavelet transform scale for signal processing. They also stated that as the number of actuator sensor pair increases in the given area, the accuracy of damage location increases. Masurkar and Yelve [19] presented extensive experimental investigations to study the interaction of Lamb wave generated using piezoelectric wafer transducers with damages in metallic, as well as composite, plates. They used the CWT to obtain information about the time of flight of the wave from the damage. This information is used in the geodesic algorithm to get the damage location. They showed that the geodesic algorithm is effective in detecting several damages in a plate, both experimentally and through finite element simulation.

Local monitoring is an SHM technique that monitors a small area immediately adjacent to the sensor. They are useful for tracking the progress of damage already identified in routine non-destructive testing (NDT) inspection, or monitoring known hot-spots [20]. The term "hot spot" is frequently used to refer to an area of high stress concentration where there is a high probability of cracking. When an external load (such as uniform tension) is applied to the plate with holes, stress concentration arises in the vicinity of holes, and cracks can appear, the growth of which can destroy the whole structure. Recently, many researchers are focused only on detection of the crack at the hole edge with the use of guided wave propagation method. Dai et al. [21] used a PZT-based active sensing method with improved sensor design to detect the porous aluminum alloy plate hole-edge corrosion. Alem et al. [22] proposed a semi-instantaneous baseline damage detection approach using guide wave propagation technique based on the premise that the fundamental symmetric mode (S_0) of Lamb waves is attenuated by passing through a crack damage. In this approach, the calculated damage index value for each sensing path passing through or near the damage is lower than other paths. Thus, it is difficult to detect the damage when the crack created at the edge of the rivet hole is not located between any of the considered sensing paths. Chiu et al. [23] presented a computational study of the interaction between the edge-guided wave and small crack on a circular hole in an aluminum plate. It is shown that edge waves traveling on the curved surface leak energy into the medium, unlike those travelling on a straight surface which do not attenuate, and the scattered field generated by their interaction with an edge crack is investigated. Andhale et al. [24] presented new algorithms to localize different types of damages in the plain and riveted aluminum specimens. In the first part of this paper, CWT is used to extract the time of arrival data from the residual response. The arrival time data of the wave reflected from the damage is used in the two arrival time difference and asteroid algorithms to locate the damage in an enclosed area. The second part of the paper deals with the localization of a faulty rivet in a riveted specimen. The responses are obtained in the cases of both healthy and faulty riveted specimens. The presence of a faulty rivet is indicated by the inflation in amplitude of the second harmonic. They proposed a new algorithm to localize the faulty rivet, using the spectral content information. Schubert Kabban et al. [25] proposed a simulation model to determine the SHM sensitive factors for SHM validation. For this purpose, the guided Lamb waves traveling through an aluminum plate were used to detect damage that stemmed from the growth of butterfly cracks from a rivet hole. The mentioned studies are mainly concerned with small holes in rivet joints. Stawiarski et al. [26] used the elastic wave propagation phenomenon to identify the size of the fatigue crack in the isotropic plate with

a relatively large circular hole. This hole is located in the geometrical center of a rectangular plate made of aluminum alloy. To measure the crack length, 14 measuring points were considered near the hole edge and around the crack. In this study, the sensors must be placed exactly around the crack. Jalalinia et al. [27] proposed a baseline-free method for damage localization in plates with a circular hole. For damage detection, they considered 24 measuring points on the upper surface of the plate which were located on a circle concentric with the middle hole. Two different variants of the system were presented by Barski and Stawiarski [28] for the detection and evaluation of radial crack length in the case of relatively large holes. The system, which demands the reference information obtained for an intact structure, provides a better estimation of the actual size of the damage. However, in the SHM system, which works without the signal from the intact structure, the maximal length of a crack is about 24 mm, which can be monitored. Also in this study, the most dangerous point at the edge of the hole where the damage may be initialized must first be predicted, and the sensors placed exactly around the crack. In some structures, it is very difficult to predict such points. The currently presented work is devoted to the problem of detecting the location of cracks at the edge of relatively large circular holes. In this work, the location of the crack created at the edge of the hole is not predictable.

Generally, the baseline data is affected by all possible scenarios such as environmental and operational effects like variations of temperature, surface moisture and load level that greatly influence response signals. Thus, it is usually difficult or even impossible to have access to the baseline data. Recently, baseline-free methods have been taken into consideration [29, 30]. In this article, a baseline-free damage detection method based on the difference between similar paths was employed to identify the location of cracks at the edge of the hole using GUWs and CWT via pitch-catch data for damage detection. Damages are defined as cracks with different lengths that may occur at different locations at the edge of the hole. A finite element model in ABAQUS is used to simulate the propagation of lamb waves in damaged plate-like structure containing a circle hole. First, GUWs were generated through applying a 5.5 cycles sinusoidal tone burst electrical potential function on simulated piezoelectric transducer (PZT) actuators. These PZTs are located at the top surface of the plate, on the circumference of circle concentric with the hole. Based on the actuator distance to sensor, 80 transmitter–receiver paths of the transducer array are divided into 20 groups, each having similar paths. Then, for each group of similar paths, the difference between the numerical signals is calculated and processed using CWT. The signals obtained from differences between similar paths contain the back-scattered reflection coming from the defect as well as from multiple scattering between the structural

defect and the boundaries. The damaged path and arrival times of Lamb waves to the sensors from the actuator via damage is calculated using wavelet coefficients computed for the residual signal. Finally, using the arrival time data and a probabilistic approach, the crack at the edge of hole is located. In each group of similar paths, although the distance of actuators or sensors related to similar paths from the edge of the hole is the same, their distance from the edges of the plate may be different (for example when the hole is not in the middle of the plate). When the transducers are located near the edges of the plate, the waves reflected from them affect the accuracy of damage detection results. In this study, the simulated PZTs are considered at different distances from the edge of the hole to examine the effect of plate edges on damage detection results.

Continuous Wavelet Transform

The CWT approach has some exclusive characteristics, such as multi-resolution properties and various basis functions for analyzing signals which can best be described as a periodic, intermittent, noisy, transient and so on. Signals can be analyzed at different frequencies with different resolutions using the multiresolution analysis (MRA) approach. In the CWT, a signal is compared with shifted and compressed (or dilated) versions of the mother wavelet function. This dilation and contraction of the mother wavelet $\psi(t)$ is controlled by the dilation parameter a and its movement along the time axis is controlled by the translation parameter b [31].

$$\psi_{a,b}(t) = \frac{1}{\sqrt{a}} \psi\left(\frac{t-b}{a}\right) \quad (1)$$

The wavelet transform of a guided wave signal $S(t)$ is a transformation that decomposes the signal into a set of basic functions obtained by dilatation and translation of a mother wavelet $\psi(t)$. The CWT of a signal $S(t)$ at a scale a and time b is calculated using the following equation:

$$W(a,b) = \frac{1}{\sqrt{a}} \int_{-\infty}^{+\infty} S(t) \psi^*\left(\frac{t-b}{a}\right) dt = \langle S(t) \cdot \psi^*(a,b) \rangle \quad (2)$$

where ψ^* is complex conjugate of ψ and $W(a,b)$ is wavelet coefficient for the wavelet $\psi_{a,b}(t)$. The symbol $\langle \cdot \rangle$ denotes the inner product.

Choosing a suitable mother wavelet function for signal processing has a significant impact on signal analysis and extraction of desired characteristics [32]. Wavelet coefficients are greater as mother wavelet is more similar to signal components. Therefore, similarity of mother wavelet and major component of analyzed signal is a criterion to select the mother wavelet. In this study, the *Morlet* wavelet (*morl*)

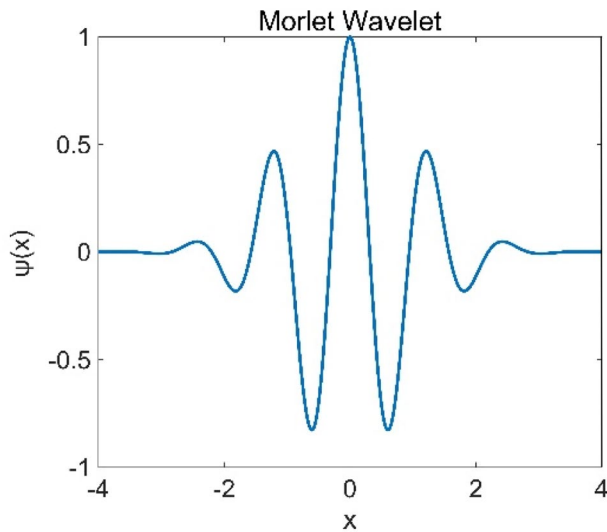


Fig. 1 The Morlet mother wavelet

(Fig. 1) is used to process the received signals, due to their closest similarity to the wave signal to be excited.

Finite Element Simulation

The propagation of Lamb waves in an isotropic plate with a circular hole was numerically simulated using the dynamic explicit time-step analysis capability of the existing standard commercial software ABAQUS. In this study, a 800 × 700 × 1.59 mm aluminum plate, with a circular hole of 40 mm radius, using 8-node standard solid element C3D8R, with three degrees of freedom per node is simulated. The center of hole is located at x -coordinate 400 mm and y -coordinate 300 mm (Fig. 2). The properties of the aluminum plate are as follows: elasticity modulus of $E=68.9$ GPa, Poisson's ratio of $\nu=0.33$ and density of $\rho=2700$ kg/m³. In this plate, through-thickness damage in the form of a crack-like notch is considered with different length and orientation at the edge of the hole and along its radius, detailed in Table 1.

To estimate the possibility of the presence of damage in the monitoring area by baseline-free methods the idea of study of the difference between signals measured in similar sensing path plays important role. In similar sensing paths, the PZT actuator-sensor distances are equal to each other. Also, the distance of piezoelectric actuators (or sensors) of these paths from the edge of the hole is equal. In other words, the paths mentioned in each group of similar paths have an equal path length and the same position to the edges of the hole. To create such paths, 16 circular piezoelectric transducers with radius 6.35 mm and thickness 0.254 mm are considered around the hole

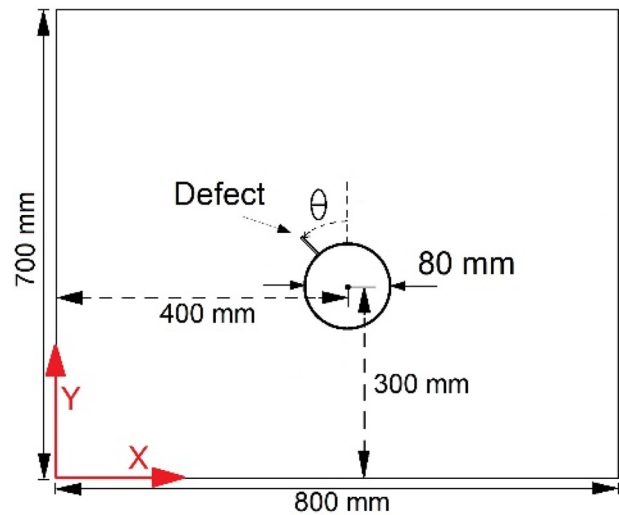


Fig. 2 Geometry of the aluminum square plate with a crack at the hole edge

Table 1 Defect input data

Crack case	Length (mm)	Orientation from y-axis	Width (mm)
1	10	0° (N)	1
2	20	0° (N)	1
3	25	10° (NE)	1
4	25	20° (NE)	1
5	25	30° (NE)	1
6	25	40° (NE)	1

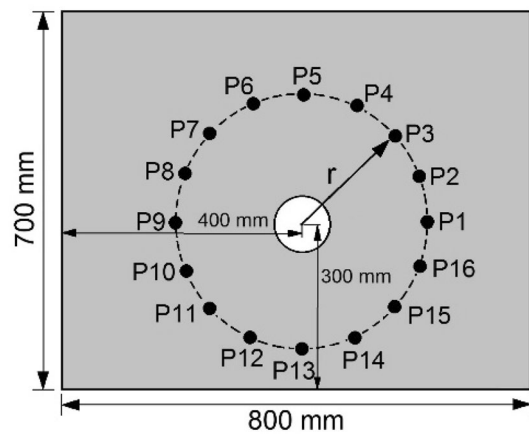


Fig. 3 Location of the measuring points in the SHM system

($P_i, i=1-16$). These transducers are placed on the circumference of a circle with the radius r ($r=100, 130, 160, 190$ or 220 mm), which has a co-center with the hole, as illustrated in Fig. 3. This simulates the presence of a

Table 2 Properties of simulated piezoelectric APC-850 [33]

Property	Symbol	Unit	APC 850
Density	ρ	kg/m ³	7700
Young's modulus	E_1, E_2	GPa	63
	E_3		54
Poisson's ratio	$\nu_{12}, \nu_{13}, \nu_{23}$		0.35
Piezoelectric coefficient	d_{31}	m/V	-175×10^{-12}
	d_{32}		-175×10^{-12}
	d_{33}		400×10^{-12}
	d_{15}		590×10^{-12}
	d_{24}		590×10^{-12}
Relative dielectric constant	$\epsilon_{33}^T / \epsilon_0$		1900

sparse array of transducers bonded into aluminum plate. The material properties of PZT transducer used in finite element simulation are reported in Table 2.

It is well known that dynamic–explicit analyses are used for simulating wave propagation in plate-like structures. On the other hand, in ABAQUS element library, piezoelectric elements can only be performed in the time integration implicit solver. Hence, the Abaqus/Stand-Explicit co-simulation can be used to overcome this deficiency. This procedure allows different solvers (implicit solver and explicit solver) to obtain the solutions in the full model [27, 34]. Figure 4 shows the flow tree of Abaqus co-simulation model, which can allow different solvers to calculate in the piezoelectric actuator and the host structure [34, 35]. As shown in this figure, the output of piezoelectric analysis will be applied as an input of the transient dynamic analysis in Abaqus/Explicit. An interaction interface is necessary to manage the data exchange in every time increment between two solvers, which is passing the data of force, displacement, strain and stress each other [35]. Also, these two analysis jobs are submitted together by creating co-execution.

The detailed information about these two kinds of models on finite element method simulation is shown in Fig. 5. To be more precise, an aluminum plate is defined as the parent model and the PZT actuator is defined as a child model. For the child model, the PZTs actuators were meshed with eight-node linear piezoelectric brick element C3D8E and applied a sinusoidal tone burst signal on the both sides of piezoelectric elements. Then, the induced strain created from the actuator was exchanged by a co-simulation interface. For the parent model, the aluminum plate was meshed with solid elements C3D8R and simulated under the Abaqus/Explicit code. This Explicit procedure was applied to simulate the wave propagation in this plate, when the induced strain was transferred from the interaction surface [35].

The Lamb waves have dispersion properties. This property causes different types of modes to be propagated in each

frequency. Dispersion curves of phase velocity and group velocity for 6061 aluminum plate are presented in Fig. 6.

The excitation signal frequency is an important parameter which should be correctly chosen to achieve more reliable damage detection results. Excitation signal frequency should be low enough, where only the first symmetric mode S_0 and the first anti-symmetric mode A_0 are propagated in the structure.

Within the low-frequency range, the wave velocity of the S_0 mode is significantly higher than that of the A_0 mode. The first symmetric mode S_0 has lower attenuation, faster propagation velocity, and lower dispersion compared to the antisymmetric mode A_0 . Both modes can be identified separately by selecting a modified signal with a narrow appropriate frequency band to excite the lamb wave. Also, as the number of cycles is reduced in a tone burst, its frequency bandwidth around the central frequency increases and Lamb mode signals are well separated. On the other hand, by increasing the number of cycles, the frequency bandwidth around the central frequency decreases and the dispersion is less. In this paper, for the excitation of the Lamb waves in the aluminum plates, a modulated 5.5 cycles sinusoidal tone burst electrical potential function with a 300-kHz center frequency and a peak-to-peak amplitude of 10 V is applied to PZT actuator (Fig. 7). For the excitation frequency $f=300$ kHz and the plate thickness of $d=1.59$ mm, the frequency–thickness product ($f \times d$) is equal to 477 kHz–mm. As shown with the vertical green dashed line in Fig. 6b, at this point, only the first fundamental symmetric S_0 and antisymmetric A_0 modes will propagate in the structure. Also, this point is excited in the low-frequency range of the dispersion curve, where the S_0 mode wave velocity is approximately twice as fast as the A_0 mode.

To create a better trade-off between the accuracy and computational time, explicit solver has been used. In dynamic time-step analysis, for an acceptable accuracy in finite element calculations, the temporal and spatial resolution of the analysis are selected appropriately. In general, the computational accuracy of the model can be improved with an increasingly smaller integration time step. A small time step increases the computation load; meanwhile, a large time step cannot resolve high frequency components. Therefore, an appropriate integration time step should be chosen. In this paper, the choice of time step (Δt) follows two criteria in Eqs. (3) and (6). Equation (3) is the Courant–Friedrichs–Lewy (CFL) condition, which dictates that the fastest propagating wave, i.e., the bulk longitudinal wave c_L , should not travel more than one element in a single time step [36, 37]. The time step calculation can be expressed as:

Fig. 4 The flow tree of Abaqus co-simulation model

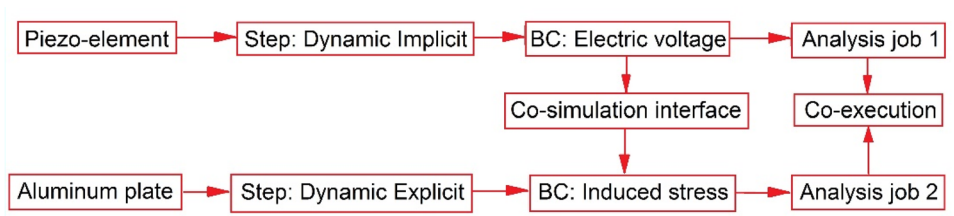


Fig. 5 Setting of a co-simulation model

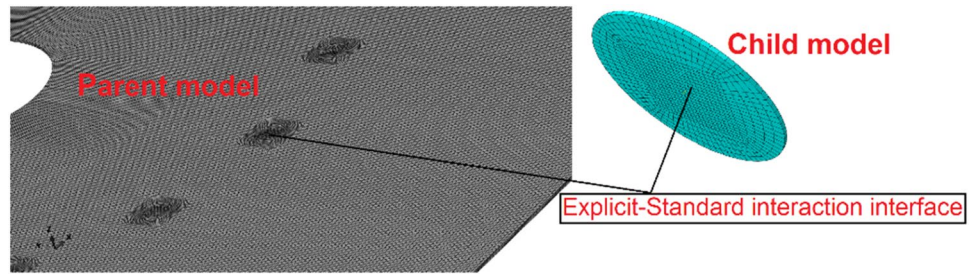


Fig. 6 **a** Phase velocity dispersion curve for the aluminum plate, **b** group velocity dispersion curve for the aluminum plate

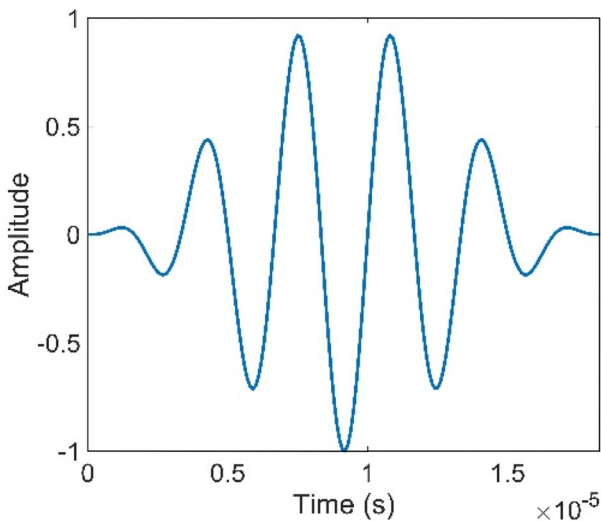
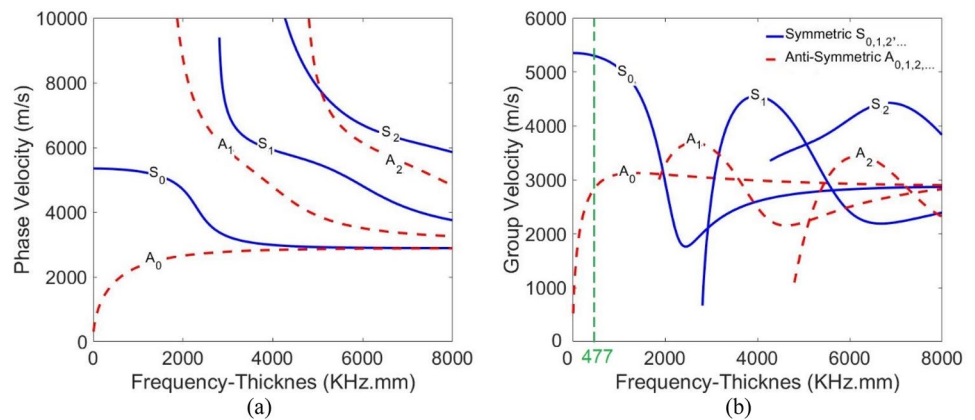


Fig. 7 5.5-cycle sinusoidal tone burst (excitation signal)

$$\Delta t \leq \frac{L_{\min}}{c_L} \tag{3}$$

where L_{\min} is the smallest dimension of the smallest finite element of the model. The longitudinal wave speed (c_L) and the transverse wave velocity (c_T) can be calculated from the following equations [37]:

$$c_L = \sqrt{\frac{E(1-\nu)}{\rho(1-2\nu)(1+\nu)}} = \sqrt{\frac{68.9 \times 10^9 \times (0.67)}{2700 \times 0.34 \times 1.33}} = 6148.93 \text{ m/s} \tag{4}$$

$$c_T = \sqrt{\frac{E}{2\rho(1+\nu)}} = \sqrt{\frac{68.9 \times 10^9}{2 \times 2700 \times 1.33}} = 3097.32 \text{ m/s} \tag{5}$$

Also, usually for a good time resolution, the minimum of 20 points per cycle at highest frequency (f_{\max}) is considered [38, 39] so that

$$\Delta t \leq \frac{1}{20f_{\max}} = \frac{1}{20 \times 300000} = 0.167 \text{ } \mu\text{s} \tag{6}$$

Also, for a good special resolution, the maximum element length L_e is limited to 10 nodes per wavelength corresponding to the highest frequency (λ_{\min}) [39, 40], which is

$$L_e \leq \frac{\lambda_{\min}}{10} \tag{7}$$

For the frequency of 300 kHz, the smallest wavelength is $\lambda_{\min} = c_T/f_{\max} = 10.3$ mm [37]. Therefore, to satisfy Eq. (7), the element size must be less than 1.03 mm. Note that the convergence and mesh refinement studies showed that the simulation of the antisymmetric mode A_0 requires a fine discretization through the sample thickness (more than three or four layers of elements through the thickness) [22, 29, 34]. Here, the element size of the mesh is considered 0.4 mm thick and 0.8 mm wide and long. The CFL condition relates the mesh size and the time step in the numerical model as mentioned in Eq. (3) [37]. Based on the CFL condition, the stable time step chosen should be less than 0.065 μ s. Therefore, the maximum time step is set to be 0.065 μ s based on Eqs. (3) and (6).

In this study, a total of 80 sensing paths, classified into 20 groups of similar paths (Table 3), are considered. In Table 3, d_1, d_2, d_3, d_4 and d_5 are actuator-sensor distances associated with similar paths introduced in groups 1–4, 5–8, 9–12, 13–16, and 17–20, respectively.

Table 3 Similar sensing paths and the geometric distances between each path

Group	Sensing path	Actuator-sensor distance (mm)
1	P1–P3, P5–P7, P9–P11, P13–P15	d_1
2	P2–P4, P6–P8, P10–P12, P14–P16	
3	P3–P5, P7–P9, P11–P13, P15–P1	
4	P4–P6, P8–P10, P12–P14, P16–P2	
5	P1–P4, P5–P8, P9–P12, P13–P16	d_2
6	P2–P5, P6–P9, P10–P13, P14–P1	
7	P3–P6, P7–10, P11–P14, P15–P2	
8	P4–P7, P8–P11, P12–P15, P16–P3	
9	P1–P5, P5–P9, P9–P13, P13–P1	d_3
10	P2–P6, P6–P10, P10–P14, P14–P2	
11	P3–P7, P7–11, P11–P15, P15–P3	
12	P4–P8, P8–P12, P12–P16, P16–P4	
13	P1–P6, P5–P10, P9–P14, P13–P2	d_4
14	P2–P7, P6–P11, P10–P15, P14–P3	
15	P3–P8, P7–12, P11–P16, P15–P4	
16	P4–P9, P8–P13, P12–P1, P16–P5	
17	P1–P7, P5–P11, P9–P15, P13–P3	d_5
18	P2–P8, P6–P12, P10–P16, P14–P4	
19	P3–P9, P7–13, P11–P1, P15–P5	
20	P4–P10, P8–P14, P12–P2, P16–P6	

For each path P_i-P_j ($i, j = 1-16$) mentioned in Table 2, when the 5.5-cycle tone burst was applied to the transducer P_i , electric potential output of sensor P_j was monitored and collected. For crack case 1, the simulated Lamb wave signals of four typical similar sensing paths mentioned in group 11 are illustrated in Fig. 8. Here, these PZTs are located on the circumference of a circle with the radius $r = 160$ mm, which has co-center with the hole. The first wave packet is mode S_0 , which travels along straight line between the PZT actuator and corresponding sensor. It can be seen that the first wave packets of these paths are similar because there is no damage in the straight line between the PZT actuator and sensor. However, in this plate, the crack located above the hole causes a fluctuation in the numerical signal recorded at P7. This fluctuation is caused by the reflection of S_0 wave mode from the damage.

Damage Identification Method

The proposed SHM system includes two parts of analysis. In the first part, the purpose is to measure the arrival time of the scattered S_0 wave mode from the damage to the sensor. The second part is responsible for identifying the location of the damage around the hole.

Part1: Feature Extraction

When the Lamb wave is produced in an actuator and travels along the damaged plate, the forward propagating wave reaches to the sensor from the direct path d_{A-S} and the scattered path $d_{A-D} + d_{D-S}$ (Fig. 9).

In this study, wavelet analysis was used to measure time delay Δt between the arrival time for S_0 mode from the direct path (first wave packet) and travel time of this mode from the actuator to the damage, and then from the damage to the sensor (scattered S_0 mode). For this purpose, first the difference between numerical signals of each group of similar paths (residual signals) is calculated. For all four similar paths that are located in each group, the six residual signals

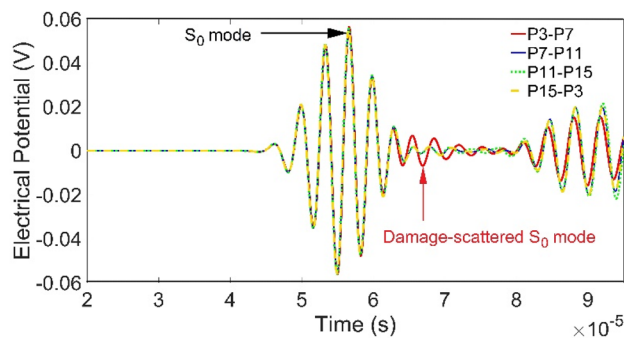


Fig. 8 Signal comparison in similar paths mentioned in group 11

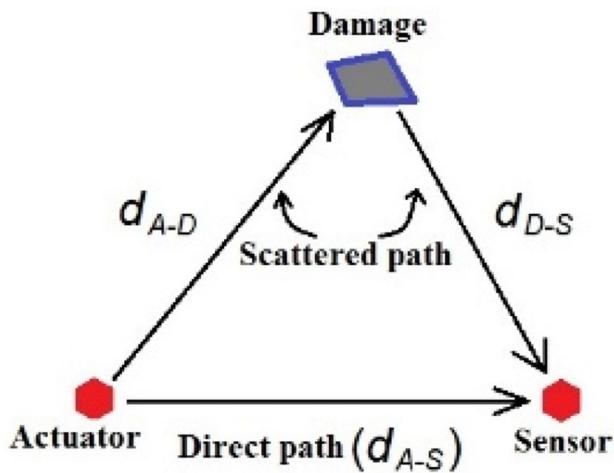


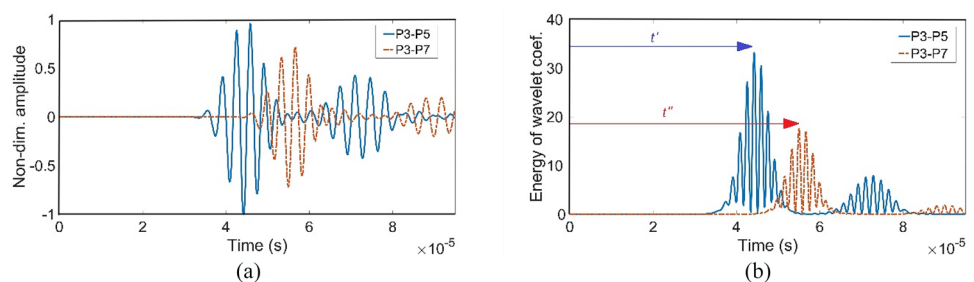
Fig. 9 Forward propagating wave in a damaged plate from actuator arrives at sensor through two paths

are measured. The residual signals contain information from the location of the damage. Then, CWT coefficients of the residual signals are computed. For each given scalogram, the amount of the scale related to the maximum value of the measured wavelet coefficients a_m was identified. Afterward, energy of the wavelet coefficients E is calculated at this scale which are drawn at the time domain, based on the following relation

$$E(a_m, b) = |W(a_m, b)|^2 \quad (8)$$

The path which produces the first maximum amplitude value of wavelet coefficients can be determined by comparing the energy of coefficients for each of the six residual signals. For this path, the time of the first peak created in the energy of the wavelet coefficients is calculated (t_2). Also, for the damaged path, the time of the first peak created in the energy of the coefficients obtained from CWT of it is calculated (t_1). The time delay Δt between the arrival time for S_0 mode from the direct path and scattered path is equal ($\Delta t = t_2 - t_1$). The reason for focusing more on the residual signals is that they contain the back-scattered reflection coming from the defect and also from multiple scattering between the structural defect and the boundaries [41].

Fig. 10 **a** Signals measured at P5 and P7, **b** Energy of the coefficients obtained from CWT of the signals measured at P5 and P7



The simulation model is first validated by calculating the group velocity of the S_0 mode by using the PZT configuration shown in Fig. 3. The transducers are located on the circumference of a circle with the radius $r = 160$ mm, which has co-center with the hole. The 5.5-cycle tone burst is applied to the transducer P3, and the transducers at P5 and P7 are used to acquire the response signals. The signals measured at P5 and P7 are plotted in Fig. 10a after converting them to the non-dimensional form by normalizing with the maximum amplitude. Then, CWT coefficients of these signals are computed. For the paths P3–P5 and P3–P7, the wavelet coefficients energy E related to the scale a_m are shown in Fig. 10b, respectively. In this figure, the first arrival peaks are the direct excitation signal S_0 at P5 and P7, received at the time $t' = 44.63 \mu\text{s}$ and $t'' = 55.04 \mu\text{s}$, respectively. Therefore, the difference between traveling time of Lamb waves from P3 to P5 and from P3 to P7 was the difference between t' and t'' , namely, $10.41 \mu\text{s}$. On the other hand, the distance between the points P3 and P5 is 122.46 mm and the distance between points the P3 and P7 is 177.78 mm. Taking into account the difference in the two traveling paths P3–P5 and P3–P7, the group velocity calculated for the S_0 mode was 5.314×10^3 m/s, which was almost the same as that obtained from the dispersion curve in Fig. 6b (green line; i.e., 5.298×10^3 m/s). Thus, the numerical model had good accuracy to calculate the Lamb wave propagation.

Next, we compare the numerical output signals of the four similar sensing paths displayed in Fig. 8. In Fig. 11, the CWT scalograms are shown for six residual signals which are calculated for these similar paths. In this figure, the row that contains the maximum value of wavelet coefficient is marked with a white line, and the energy of the coefficients placed in this row are drawn in Fig. 12a.

As shown in this figure, among the similar paths considered, the first peak is created in the wavelet coefficients energy of difference between the response signal of the path P3–P7 with the response signals of other paths (RS[(P3–P7)&(P7–P11)], RS[(P3–P7)&(P11–P15)] and RS[(P3–P7)&(P15–P3)]). Because the scattered waves from the damage have little effect on signals P7–P11, P11–P15 and P15–P3, the signals measured for these similar paths are almost identical and the difference between them is close to zero. However, when tone burst is applied on P3, the scattered S_0 mode from damage affect the signal measured at P7

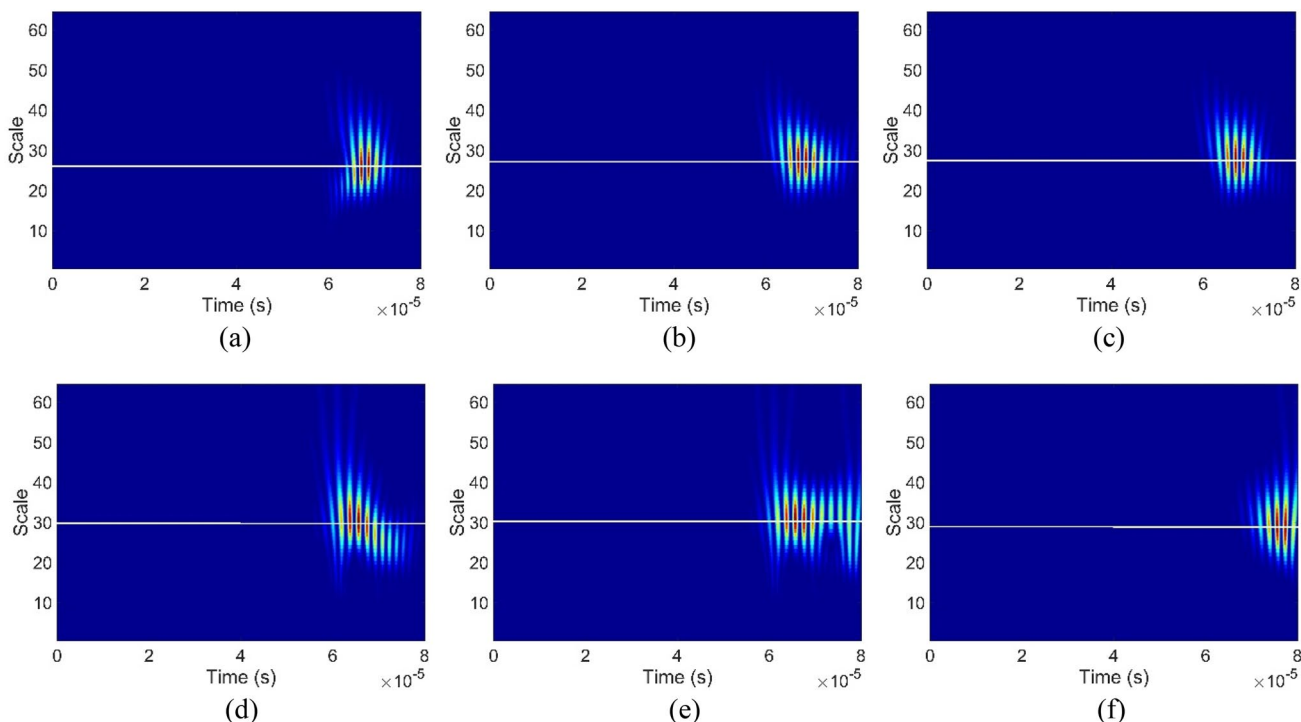


Fig. 11 Wavelet scalograms associated with residual signals obtained from difference between two similar paths **a** P3–P7 and P7–P11, **b** P3–P7 and P11–P15, **c** P3–P7 and P15–P3, **d** P7–P11 and P11–P15, **e** P7–P11 and P15–P3, **f** P11–P15 and P15–P3

(see Fig. 8). Thus, there is an obvious difference between the measured signals of path P3–P7 and other similar paths mentioned in group 11, which is caused by damage scattering, so this path is considered as the damaged path. Before this peak, energy of the wavelet coefficients calculated for each six residual signals has the values close to zero, since in this period the obtained numerical signals at simulated PZT sensors are almost identical. The results demonstrate that this approach can identify the damaged path without considering the data taken from a pristine plate. In Fig. 12a, the time of the first peak created in the energy of the wavelet coefficients is denoted by t_2 . Also, the energy of the coefficients obtained from CWT of the path P3–P7 at scale a_m is shown in Fig. 12b. In this figure, the time corresponding to the beginning the non-zero point of the first peak is the arrival time of the direct wave, denoted by t_1 [42]. In practice, it is difficult to identify this non-zero point due to the noise in the signals. In Fig. 12b, the time of the first peak created in the energy of the wavelet coefficients is denoted by t_1 . The time delay Δt between the arrival time for S_0 mode from the direct path d_{P3-P7} and scattered path $d_{P3-D} + d_{D-P7}$ is equal ($\Delta t = t_2 - t_1$). The same procedure is repeated for the other groups of similar paths, and the time delay Δt is

calculated. Then for each group of similar paths i , the following feature ratio (FR) is computed

$$FR_i = \frac{F_i^d}{F_{\max}^d} \begin{cases} \text{for } d = d_1 & i = 1 - 4 \\ \text{for } d = d_2 & i = 5 - 8 \\ \text{for } d = d_3 & i = 9 - 12 \\ \text{for } d = d_4 & i = 13 - 16 \\ \text{for } d = d_5 & i = 17 - 20 \end{cases} \quad (9)$$

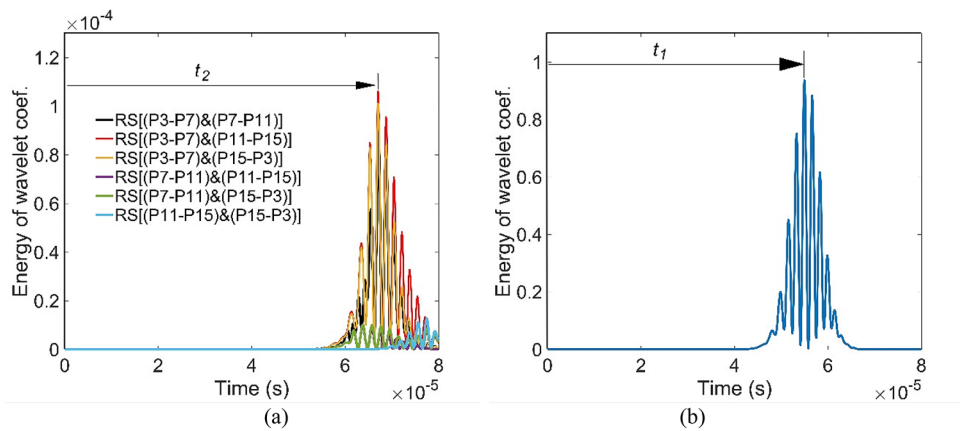
where

$$F_i^d = \max [E_{ij}^d(a_m, t_2)] \quad i = 1, 2, \dots, 20 \quad j = 1, 2, \dots, 6 \quad (10)$$

$$F_{\max}^d = \max(F_i^d) \quad (11)$$

where d is actuator-sensor distance associated with i th group of similar paths, and j represents the j th residual signal which is calculated for this group. In the next part, it has been explained how to identify the location of the damage, using the obtained results in this part.

Fig. 12 **a** Energy of wavelet coefficient associated with residual signals measured for the four similar paths mentioned in group 1, at selected scale, **b** energy of the coefficients obtained from CWT of the path P3–P7



PART2: Damage Detection Using Feature Extraction

When the wave packet encounters damage, reflection and scattering occur. The waves always select the minimum energy path to move between two points. On a plate-like structure, consider the actuator *A* and the sensor *S*, which is located at (A_x, A_y) and (S_x, S_y) , respectively. In this plate, if there is a damage *D* with coordinates (D_x, D_y) then the distance between the actuator *A* and damage *D* is given by:

$$d_{A-D} = \sqrt{(A_x - D_x)^2 + (A_y - D_y)^2} \tag{12}$$

The distance between damage *D* and the sensor *S* is as follows

$$d_{D-S} = \sqrt{(D_x - S_x)^2 + (D_y - S_y)^2} \tag{13}$$

And the distance between the actuator node *A* and the sensor node *S* is given by:

$$d_{A-S} = \sqrt{(A_x - S_x)^2 + (A_y - S_y)^2} \tag{14}$$

If t_{A-D} , t_{D-S} and t_{A-S} are the time of flight from the actuator *A* to the sensor *S*, the time of flight from damage *D* and from the actuator *A* to the sensor node *S*, respectively, then Eqs. (12)–(14) can be written as

$$d_{A-D} = V_{S0} t_{A-D} \tag{15}$$

$$d_{D-S} = V_{S0} t_{D-S} \tag{16}$$

$$d_{A-S} = V_{S0} t_{A-S} \tag{17}$$

where V_{S0} is the group velocity of the S_0 Lamb wave mode. We can obtain the time delay Δt for the sensor *S* from

$$\frac{d_{A-D} + d_{D-S}}{V_{S0}} - \frac{d_{A-S}}{V_{S0}} = t_{A-D} + t_{D-S} - t_{A-S} = \Delta t \tag{18}$$

Thus, the wave travel time from the actuator *A* to damage *D*, and then from damage *D* to the sensor *S* is determined as

$$\begin{aligned} & \sqrt{(A_x - D_x)^2 + (A_y - D_y)^2} + \\ & \sqrt{(D_x - S_x)^2 + (D_y - S_y)^2} \\ & = (\Delta t \cdot V_{S0}) + d_{A-S} \end{aligned} \tag{19}$$

In this part, the purpose is to identify the location of the defect (D_x, D_y) . First, for each group of similar paths presented in Table 3, damaged path and the time delay Δt between the arrival time for S_0 mode from the direct path and scattered path are obtained using the method mentioned in the previous part. The plate is then divided into 1×1 mm elements. The damage present probability $P(x,y)$ at the each node position (x,y) was defined as follows:

$$P(x,y) = \sum_{i=1}^K FR_i \exp \left[- \left(\frac{R_i(x,y)}{\beta} \right)^2 \right] \tag{20}$$

where K is the number of groups mentioned in Table 3, FR_i is feature ratio of the i th group that is calculated by Eq. (9), and $R_i(x,y)$ is defined as the relative distance of the node (x,y) to the actuator and sensor associated with i th path which is detected in the previous part as the damaged path, that is

$$\begin{aligned} & R_i(x,y) \\ & = \frac{\sqrt{((A_x)_i - x)^2 + ((A_y)_i - y)^2} + \sqrt{(x - (S_x)_i)^2 + (y - (S_y)_i)^2}}{(\Delta t_i \cdot V_{S0}) + d_{A-S}} - 1 \end{aligned} \tag{21}$$

In this equation, $(A_x, A_y)_i$ and $(S_x, S_y)_i$ are the coordinates of simulated PZT actuator and sensor, respectively, and Δt_i is the time delay computed for the i th damaged path. In the

Fig. 13 Corrupting the original data using white Gaussian noise of SNR = 10 dB. The received signal in sensing paths **a** P3–P7 and **b** P11–P15

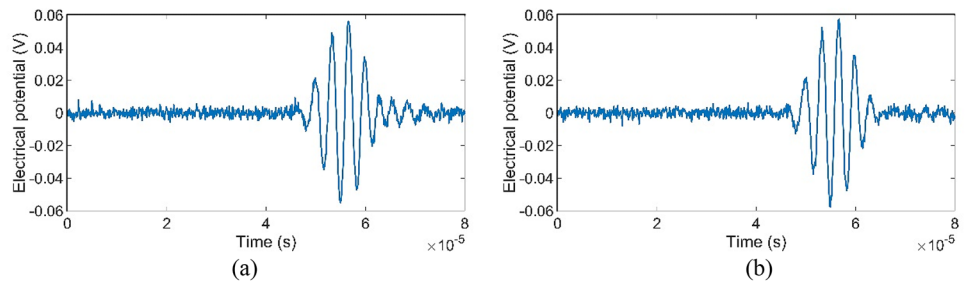


Fig. 14 Damage detection results obtained for crack case 1 when the transducers are placed on the circumference of a circle with the radius **a** $r=100$ mm, **b** $r=130$ mm, **c** $r=160$ mm, **d** $r=190$ mm, **e** $r=220$ mm

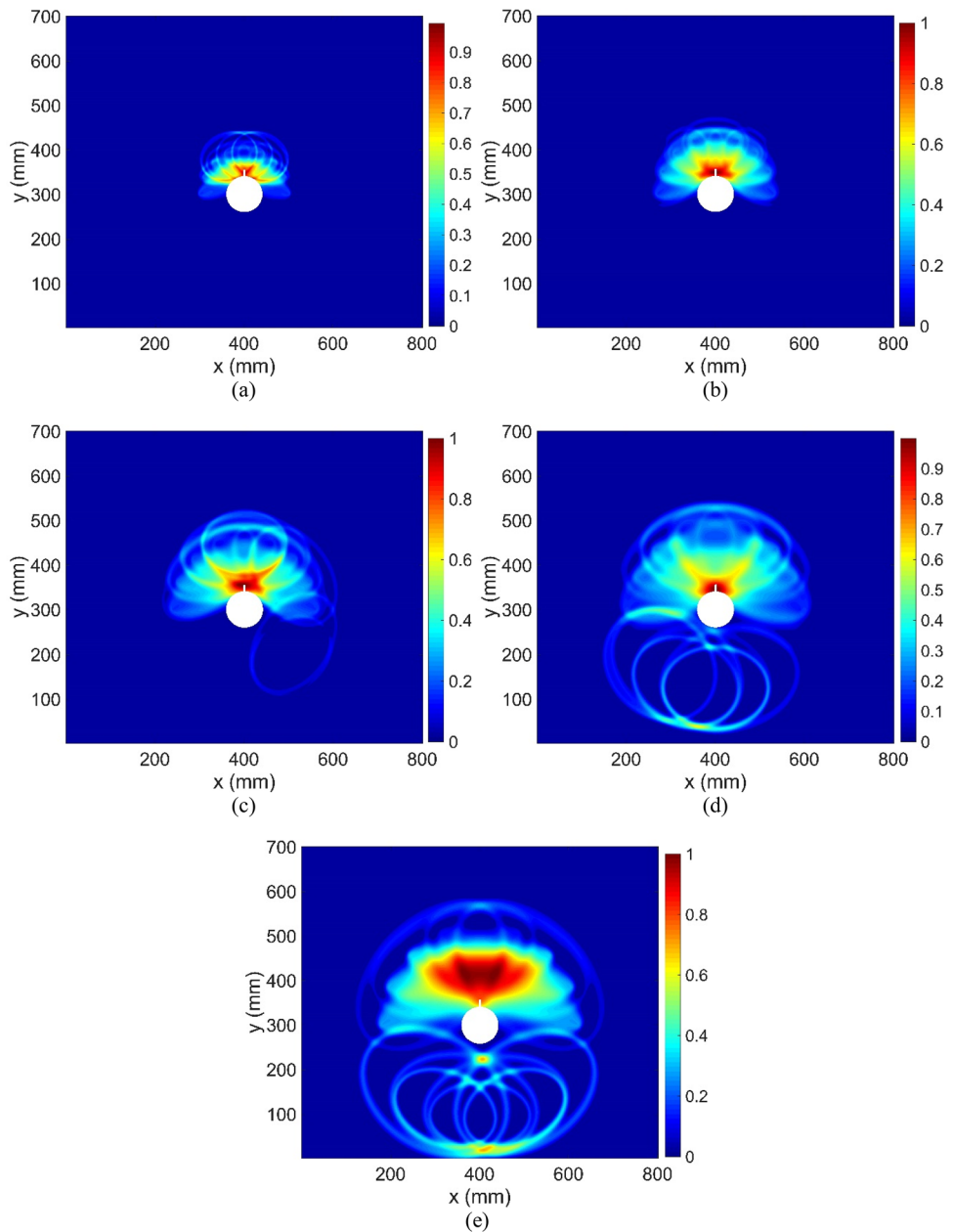
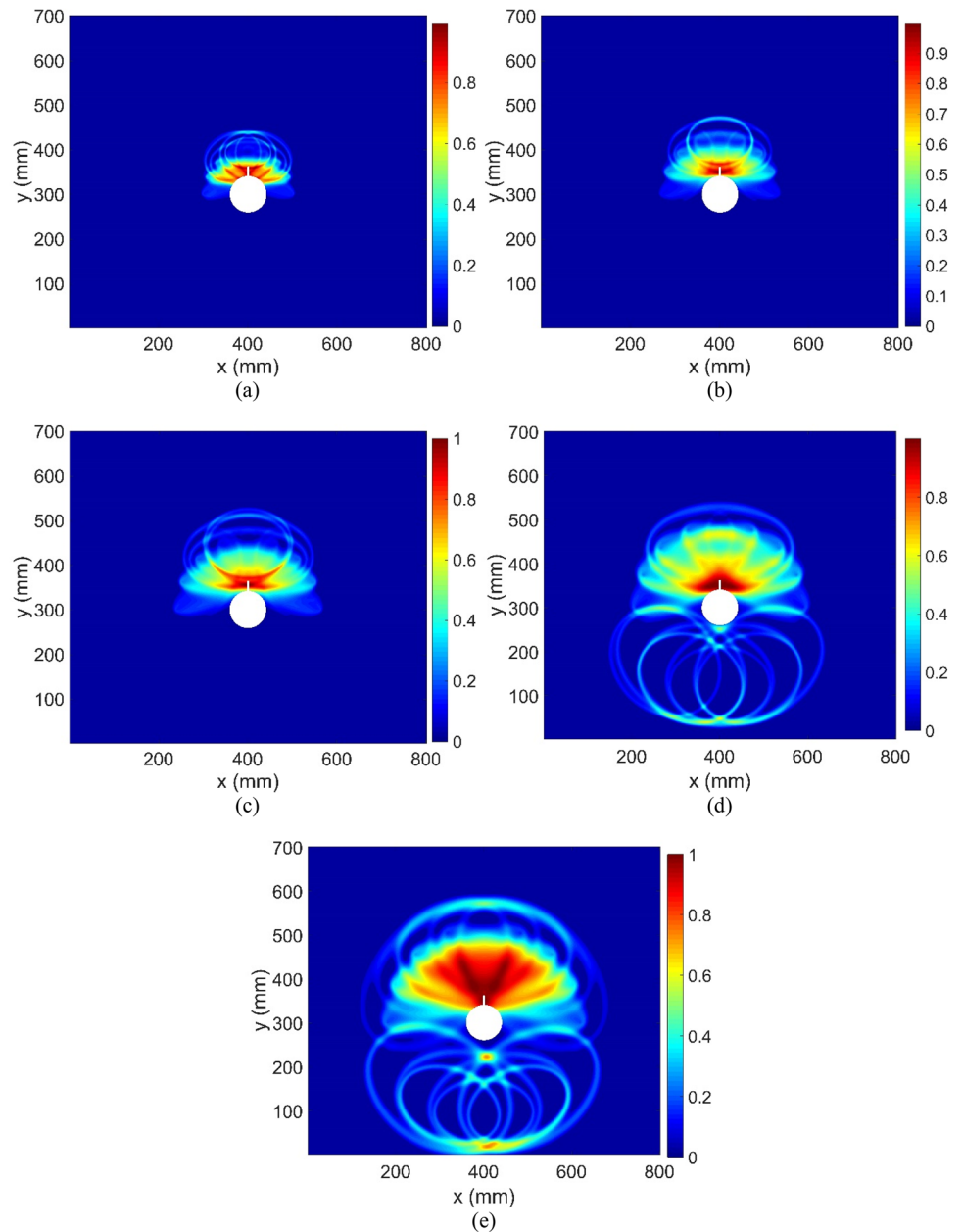


plate-like structure, the locus of points whose the sum of the distance from the actuator A and the sensor S is constant ($\Delta t_i \cdot V_{S0} + d_{A-S}$) is a curve. The relative distance is zero at

any grid node (x, y) located along this curve, and it linearly increases at locations away from it. Constant β is the influence region of the curve drawn for the possible locations of

Fig. 15 Damage detection results obtained for crack case 2 when the transducers are placed on the circumference of a circle with the radius **a** $r=100$ mm, **b** $r=130$ mm, **c** $r=160$ mm, **d** $r=190$ mm, **e** $r=220$ mm



the damage. Coefficient β has been determined by trial and error. A small β reduces the zone of influence of the curve that shows possible damage locations in the plate, so that flaws near the curve might go undetected. On the other hand, a large β may cause unwanted overlap among different curves measured for groups of similar paths. In this study, $\beta=0.04$ provided an appropriate trade-off between sensitivity to damage and the broad coverage area.

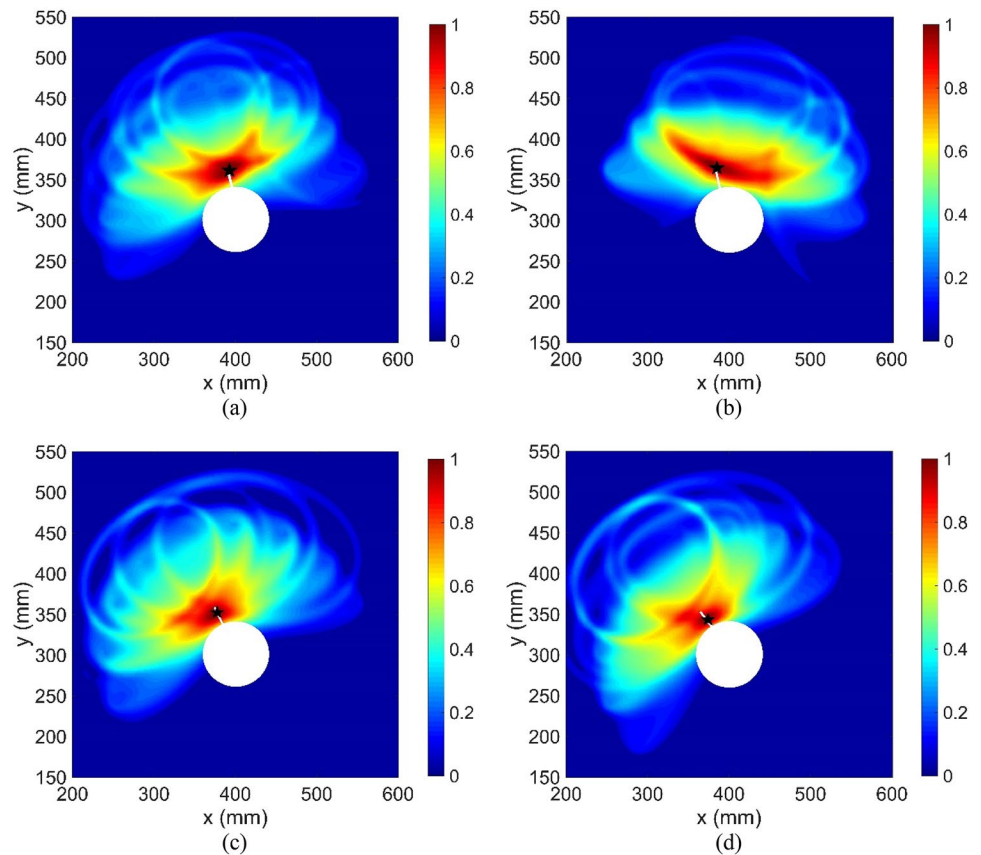
Finally, at each node (x, y) , the discontinuity Index DI is defined as follows

$$DI(x, y) = \frac{P_{\max}(x, y) - P(x, y)}{P_{\max}(x, y)} \quad (22)$$

where $P_{\max}(x, y)$ is the maximum value of $P(x, y)$ obtained on the damaged aluminum plate, with a hole.

In real monitoring systems, the Lamb wave signals recorded by sensors are often polluted by noise which directly affect their accuracy of measurement. For simulation purposes the numerical data is polluted with noise using the procedure applied in [43–45] in which the presented methods were also verified numerically. To simulate the practical field signal, the Gaussian white noise with a level of $SNR = 10$ dB is added to the simulation results of output

Fig. 16 Damage detection results obtained for **a** crack case 3, **b** crack case 4, **c** crack case 5, **d** crack case 6



signals for all paths mentioned in Table 3. As an example, the received signal in sensing paths P3–P7 and P11–P15 with added white Gaussian noise of SNR = 10 dB is shown in Fig. 13.

Simulation Results and Discussion

Identification of Single Crack

For the damage scenario of case 1, the images of the probability distribution for the location of the defect are illustrated in Fig. 14a–e when the 16 transducers are placed on the circumference of a circle with the radius 100, 130, 160, 190 or 220 mm, respectively. The contour plot describes the values of DI obtained from analysis of the all paths mentioned in the Table 3. In all figures, the white line drawn at the edge of the hole indicates the location and size of crack. As observed in Fig. 14a–c, when the transducers are close to the edge of the hole and away from the edges of the plate, the values of DI obtained from the analysis of similar paths can well identify the location of the crack. However, as shown in

Fig. 14d and e, as the PZTs are located near the edge of the plate, the DI values obtained near the bottom edge increase, which are closer to the PZTs than to the other edges. This is because in the signals measured for some groups of similar paths, the wave reflected from this edge reaches the simulated PZT sensors faster than the wave reflecting from the crack does. Hence, although with increasing r , the density of transducers decreases while the monitoring area increases, the proximity of transducers to the edges of the plate and the effect of these edges in the measured signals for some paths cause error in detecting the damage location.

Figure 15 represents the damage detection results of crack length 20 mm (damage scenario of case2), which shows a similar behavior to the damage scenario of case 1 in which the crack length was 10 mm. Note that the applied method of case 2 is similar to case 1.

For the damage scenario of cases 3–6, the damage map of the plate in terms of the DI defined in Eq. (22) is shown in Fig. 16(a)–d when 16 transducers are placed on the circumference of a circle with the radius 160 mm. Here, the performance of the proposed algorithm in identifying radial

crack with four different orientations is investigated. The predicted point with maximum DI is shown by a black star. Figure 16 shows that the proposed baseline free method can effectively identify the location of cracks created at the edge of the hole.

Identification of Multiple Crack

The previous part proved that the proposed method can efficiently locate a crack with different lengths and various orientations at the hole edge. In the next two examples, the performance of the recommended method in determining multiple cracks appearing at the edge of the hole is investigated. For this purpose, an aluminum plate with two damage states is considered. In each damage state, two through-thickness cracks with different lengths and various orientations measured counterclockwise from the y-axis are considered as listed in Table 4. The width of all cracks is identical and equal to 1 mm. In Fig. 17, the location of the cracks is illustrated schematically in the damaged plate.

For the first and second damage states, the map of the plate in terms of the DI computed using Eq. (22) is shown in Fig. 18a and b, respectively, when 16 transducers are placed on the circumference of a circle with the radius 160 mm. For these damage states, the values of FR calculated according to Eq. (9) for all groups of similar paths are shown in Table 5. According to the results shown in Table 5, for groups 1–4, the FR value obtained for paths P10–P12 and P4–P6 is 1 and 0.92, respectively; however, it is close to zero for the other groups, which demonstrates the existence of damage around these paths. For the similar paths introduced in groups 5–8, 9–12, and 13–16, the FR values obtained for paths located around the crack with 135° orientation (e.g. P9–P12, P9–P13 and P9–P14) are greater than the FR values obtained for the paths located around the other crack (e.g. P3–P6, P3–P7 and P3–P8). Thus, for these similar paths, the larger the crack length, the greater the effect of the wave scattered from crack on the measured signals. Also, for groups 17–20, wave scattered from the longer crack has a significant effect on the measured signal of the paths P9–P15, P7–P13, and P8–P14, while the effect of the wave scattered from the shorter crack is detectable only in the numerical signal of P2–P8. Thus,

In Fig. 18a, the values of DI obtained at the location of both cracks are larger than other locations. Furthermore, the area around the 135° orientation crack is darker than the around the 0° orientation crack, indicating more severe damage.

In the second damage state, for the similar paths introduced in groups 1–4, the FR values obtained for paths P4–P6, and P2–P4 which are located above smaller crack and longer crack, respectively, are significantly higher than the FR values obtained for other paths. For groups 5–8, the waves scattered from both cracks have the greatest effect on the measured signal of the path P3–P6. For the similar paths mentioned in groups 9–12, 13–16 and 17–20, the FR values obtained for paths located around the cracks are larger than for the other paths mentioned in these groups. Furthermore, according to the results shown in Fig. 18b, it can be inferred that the DI values obtained after analyzing paths mentioned in the Table 3 can locate the cracked area with acceptable accuracy.

Accordingly, it can be concluded that in the case of the two cracks at the edge of the hole, the proposed baseline-free method can accurately identify the location of both cracks.

The Effects of the Uncertainties of Transducers Dislocation

As described before, this study proposed a baseline free defect identification method based on the difference between similar paths. The sensor spacing of transmitter–receiver paths had to be equal in these similar paths. Also, the distance of piezoelectric actuators (or sensors) of these paths from the edge of the hole is equal. The signals obtained from the differences between the similar paths contain the back-scattered reflection coming from the defect. In each group of similar paths, if the distance between the actuators and the sensors is not the same, then the proposed method may not be able to correctly identify the crack location and the arrival time of the scattered S_0 wave mode from the damage to the sensor. Here, for the damage scenario of case 2 ($r = 160$ mm), the effects of uncertainty in the length of similar paths which could be due to the inaccuracy in the installation of sensors on plate, on the accuracy of damage detection results are investigated. The amount of this dislocation depends on the operator and also relies on the usual sheet metal manufacturing tolerances (about 0.5 mm) [46]. Alam et al. [46] investigated the influence of uncertainties in the length of sensing paths on the accuracy of instantaneous damage identification results for the dislocations smaller than 2 mm. To examine the sensitivity of the proposed method to the uncertainties of the transducers dislocation,

Table 4 Damage input data

Damage state	Crack size (mm)	Crack orientation
1	10	0°
	15	135°
2	10	0°
	15	– 35°

Fig. 17 Geometry of an aluminum square plate with two cracks at the hole edge: **a** damage state 1, **b** damage state 2

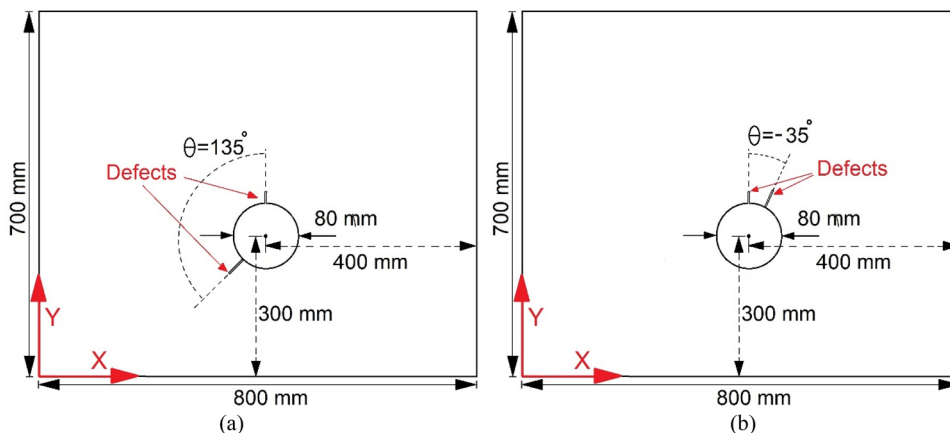


Fig. 18 The damage detection results on the aluminum plate with two cracks at the hole edge: **a** damage state 1, **b** damage state 2

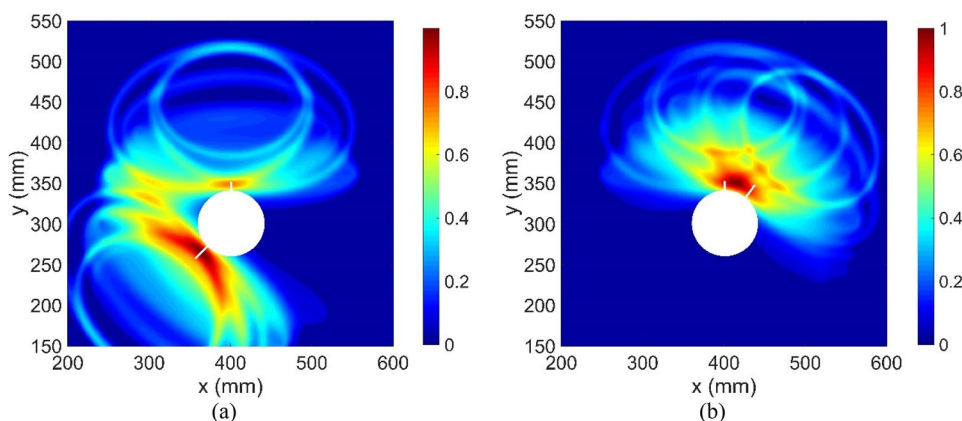


Table 5 The values of FR calculated according to Eq. (9) for the first and second damage states

Group	Damage state 1		Damage state 2	
	Damaged path	FR	Damaged path	FR
1	P9–P11	0.08	P5–P7	0.03
2	P10–P12	1	P2–P4	1
3	P11–P13	0.06	P3–P5	0.16
4	P4–P6	0.92	P4–P6	0.93
5	P9–P12	1	P1–P4	0.48
6	P10–P13	0.68	P2–P5	0.53
7	P3–P6	0.84	P3–P6	1
8	P4–P7	0.57	P4–P7	0.81
9	P9–P13	1	P1–P5	1
10	P10–P14	0.36	P2–P6	0.76
11	P3–P7	0.67	P3–P7	0.38
12	P4–P8	0.27	P4–P8	0.32
13	P9–P14	1	P1–P6	1
14	P2–P7	0.54	P2–P7	0.76
15	P3–P8	0.74	P3–P8	0.6
16	P8–P13	0.61	P4–P9	0.18
17	P9–P15	0.4	P1–P7	1
18	P2–P8	0.86	P2–P8	0.79
19	P7–P13	0.5	P15–P5	0.5
20	P8–P14	1	P16–P6	0.62

four transducers dislocation scenarios are considered as follows:

Scenario 1. The dislocation for transducers P1, P2, P3, P4, P5 is considered to be equal to 2 mm to the right, and for transducers P6, P7, P8, P9 is 2 mm to the left (see Fig. 19a).

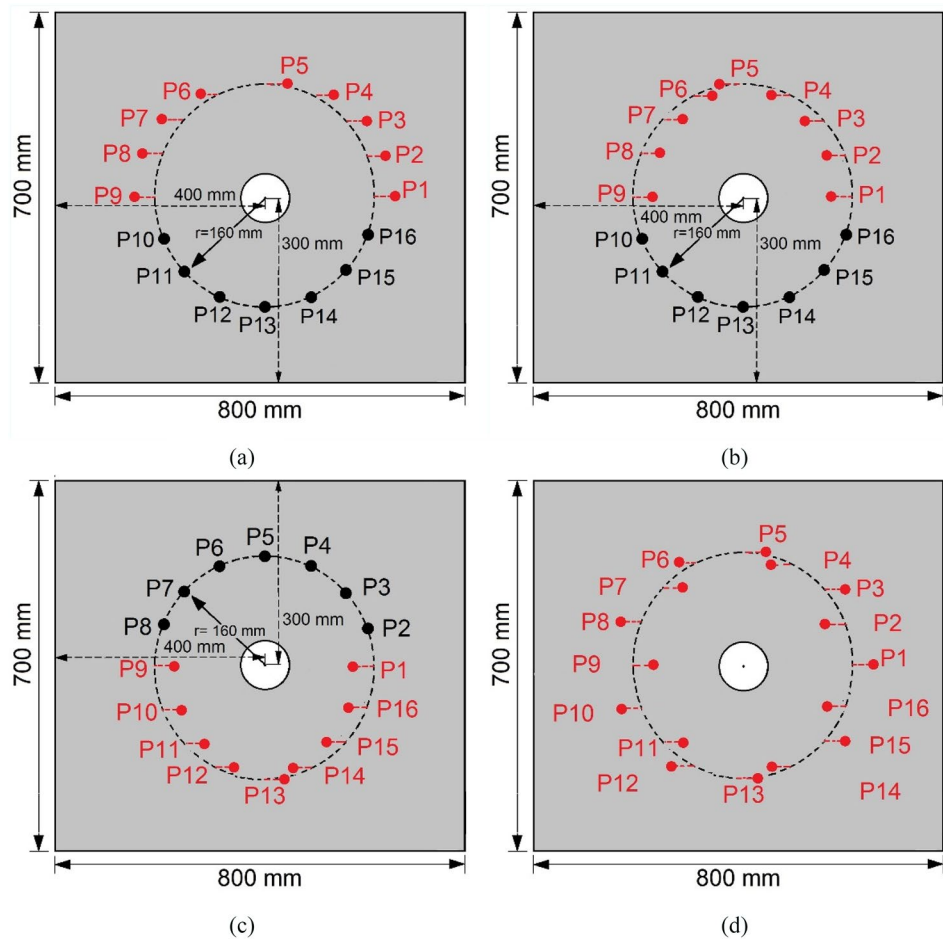
Scenario 2. The dislocation for transducers P1, P2, P3, P4, P5 is considered to be equal to 2 mm to the left, and for transducers P6, P7, P8, P9 is 2 mm to the right (see Fig. 19b).

Scenario 3. The dislocation for transducers P9, P10, P11, P12, P13 is considered to be equal to 2 mm to the right, and for transducers P1, P14, P15, P16 is 2 mm to the left (see Fig. 19c).

Scenario 4. The dislocation for transducers P1, P3, P5, P7, P9, P11, P13, P15 is considered to be equal to 2 mm to the right, and for transducers P2, P4, P6, P8, P10, P12, P14, P16 is 2 mm to the left (see Fig. 19d).

For the transducers dislocation scenarios 1–4, the images of the probability distribution for the location of the defect are illustrated in Fig. 20a–d, respectively, when the 16 transducers are placed on the circumference of a circle with the radius 160 mm. The predicted point with maximum DI is shown by a black star. For the first and third transducers dislocation scenarios, although the DI values obtained around

Fig. 19 **a** First transducers dislocation scenario, **b** second transducers dislocation scenario, **c** third transducers dislocation scenario, **d** fourth transducers dislocation scenario



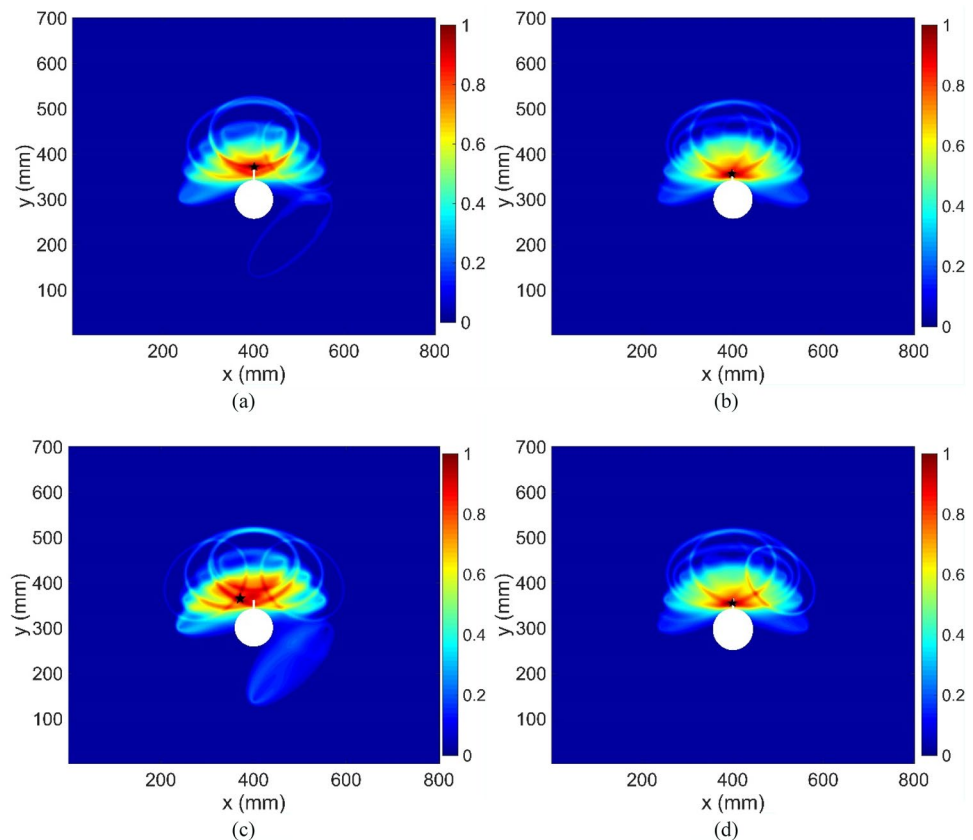
the crack are larger than in other places, the maximum DI computed using Eq. (22) is not precisely located in the actual damage (see Fig. 20a, c). Also, the comparison of Fig. 20b, d and Fig. 15c show some differences that are not significant. Therefore, it can be said that for the second and fourth transducers dislocation scenarios, the proposed damage detection method is not sensitive to dislocation of transducers. According to the results shown in Fig. 20, it can be said that the inaccuracy in the installation of the transducers has caused a small error in measuring the arrival time of the scattered S_0 and detecting the damaged path. However, for these transducers dislocation scenarios, the proposed damage detection method is not sensitive to dislocation of transducers which can occur through installation process, and the DI values can detect the damage location with acceptable accuracy.

Conclusion

The paper presents a baseline free approach based on damage-scattered signals for SHM of isotropic plate with a circular hole by means of GUVs and signal processing. The

numerical simulations conducted in ABAQUS and GUVs were generated by simulating 16 transducers capable of generating and identifying the propagation of the Lamb wave. The locations of transducers on the plate were set in a way that traveling waves have similar paths from actuators to the sensors. By comparing the measured signal in similar paths, a crack with different length and orientation at the edge of the hole can be detected irrespective of data taken from a pristine plate. To detect the location of hole-edge cracks, 80 sensing paths were considered with four different lengths. These paths are divided into 20 groups with each group having similar paths. To identify the damage, for each group of similar paths, the difference between the numerical signals (residual signals) was initially measured. Next, by applying CWT on the residual signals, the path with the shortest time of flight from the actuator to damage and then from damage to the sensor has been detected. Also, by using the coefficients obtained from the wavelet transform, it is possible to measure duration of time Lamb wave sent from the actuator reaches the damage and then the sensor. Finally, using the arrival time data and a probabilistic approach, the location of crack at the edge of central hole is well detected. In each group of similar paths, when the distance of actuators or

Fig. 20 Damage detection results obtained for the **a** first transducers dislocation scenario, **b** second transducers dislocation scenario, **c** third transducers dislocation scenario, **d** fourth transducers dislocation scenario



sensors related to similar paths from the edges of the plate is the same, the proposed method can identify the location of the crack accurately. However for the similar paths mentioned in each group when this distance is different, the wave reflected from the edges of the plate may affect the damage detection results. In this case, if the transducers are placed near the edges of the plate, in some similar paths, the wave reflected from the edge of the plate reaches the sensor location faster than the wave scattered from the damage does. Thus, in order to accurately identify the damage location, the distance of the transducers from the edge of the hole should be less than their distance from the edges of the plate. However, by ignoring the *DI* values obtained at the edges of the plate and limiting the monitoring area to the circular surface between the transducers, it can be stated that even when the transducers are located near the edges of the plate, the proposed method can detect the crack location at the edge of the hole. In the case where there are two cracks at the hole edge, for each group of similar paths, the FR values obtained for paths located around the cracks are larger than the other paths mentioned in these groups. Thus, the results obtained from the analysis of similar paths can accurately identify the location of both cracks. However, this approach does not provide reliable information about the real crack length or the number of cracks. The results are promising

and future studies should focus on the experimental validation of the methodology.

References

1. Rao GR, Davis TT, Sreekala R, Gopalakrishnan N, Iyer NR, Lakshmanan N (2015) Damage identification through wave propagation and vibration based methodology for an axial structural element. *J Vib Eng Technol* 3(4):383–399
2. Zhao J, Miao X, Li F, Li H (2018) Probabilistic diagnostic algorithm-based damage detection for plates with non-uniform sections using the improved weight function. *J Vib Eng Technol* 6(3):249–260
3. Bourasseau N, Moulin E, Delebarre C, Bonniau P (2000) Radome health monitoring with Lamb waves: experimental approach. *NDT E Int* 33(6):393–400
4. Mei H, Migot A, Haider MF, Joseph R, Bhuiyan MY, Giurgiutiu V (2019) Vibration-based in-situ detection and quantification of delamination in composite plates. *Sensors* 19(7):1734
5. Alleyne DN, Pavlakovic B, Lowe MJS, Cawley P (2004) Rapid, long range inspection of chemical plant pipework using guided waves. *Key Eng Mater* 270:434–441
6. Tua PS, Quek ST, Wang Q (2005) Detection of cracks in cylindrical pipes and plates using piezo-actuated Lamb waves. *Smart Mater Struct* 14(6):1325
7. Sohn H, Park HW, Law KH, Farrar CR (2007) Damage detection in composite plates by using an enhanced time reversal method. *J Aerosp Eng* 20(3):141–151

8. Masurkar FA, Yelve NP (2017) Optimizing location of damage within an enclosed area defined by an algorithm based on the Lamb wave response data. *Appl Acoust* 120:98–110
9. Poddar B, Bijudas CR, Mitra M, Mujumdar PM (2012) Damage detection in a woven-fabric composite laminate using time-reversed Lamb wave. *Struct Health Monit* 11(5):602–612
10. Wang X, Peter WT, Mechefske CK, Hua M (2010) Experimental investigation of reflection in guided wave-based inspection for the characterization of pipeline defects. *NDT E Int* 43(4):365–374
11. Rose JL (2004) Ultrasonic guided waves in structural health monitoring. *Key Eng Mater* 270:14–21
12. Lanza Discalea F, Matt H, Bartoli I, Coccia S, Park G, Farrar C (2007) Health monitoring of UAV wing skin-to-spar joints using guided waves and macro fiber composite transducers. *J Intell Mater Syst Struct* 18(4):373–388
13. Rizzo P, di Scalea FL (2006) Feature extraction for defect detection in strands by guided ultrasonic waves. *Struct Health Monit* 5(3):297–308
14. Paget CA, Grondel S, Levin K, Delebarre C (2003) Damage assessment in composites by Lamb waves and wavelet coefficients. *Smart Mater Struct* 12(3):393
15. Rizzo P, Sorrivi E, di Scalea FL, Viola E (2007) Wavelet-based outlier analysis for guided wave structural monitoring: application to multi-wire strands. *J Sound Vib* 307(1–2):52–68
16. Su Z, Ye L, Bu X (2002) A damage identification technique for CF/EP composite laminates using distributed piezoelectric transducers. *Compos Struct* 57(1–4):465–471
17. Yelve NP, Rode S, Das P, Khanolkar P (2019) Some new algorithms for locating a damage in thin plates using lamb waves. *Eng Res Express* 1(1):015027
18. Wang D, Ye L, Su Z, Lu Y, Li F, Meng G (2010) Probabilistic damage identification based on correlation analysis using guided wave signals in aluminum plates. *Struct Health Monit* 9(2):133–144
19. Masurkar FA, Yelve NP (2017) Lamb wave based experimental and finite element simulation studies for damage detection in an aluminium and a composite plate using geodesic algorithm. *Int J Acoust Vib* 22(4):413–421
20. Cawley P (2018) Structural health monitoring: closing the gap between research and industrial deployment. *Struct Health Monit* 17(5):1225–1244
21. Dai W, Wang X, Zhang M, Zhang W, Wang R (2019) Corrosion monitoring method of porous aluminum alloy plate hole edges based on piezoelectric sensors. *Sensors* 19(5):1106
22. Alem B, Abedian A (2018) A semi-baseline damage identification approach for complex structures using energy ratio correction technique. *Struct Control Health Monit* 25(2):e2103
23. Chiu WK, Rose LRF, Vien BS (2017) Scattering of the edge-guided wave by an edge crack at a circular hole in an isotropic plate. *Procedia Engineering* 188:309–316
24. Andhale YS, Masurkar F, Yelve N (2019) Localization of damages in plain and riveted aluminium specimens using lamb waves. *Int J Acoust Vib* 24:1
25. Schubert Kabban C, Uber R, Lin K, Lin B, Bhuiyan MY, Giurgiutiu V (2018) Uncertainty evaluation in the design of structural health monitoring systems for damage detection. *Aerospace* 5(2):45
26. Stawiarski A, Barski M, Pająk P (2017) Fatigue crack detection and identification by the elastic wave propagation method. *Mech Syst Signal Process* 89:119–130
27. Jalalinia M, Amiri GG, Razzaghi SAS (2022) Output-only method for defect identification in the internal edge of the plates with a circular hole using guided ultrasonic waves and discrete wavelet transform. *Iran J Sci Technol Trans Civ Eng* 2022:1–23
28. Barski M, Stawiarski A (2018) The crack detection and evaluation by elastic wave propagation in open hole structures for aerospace application. *Aerosp Sci Technol* 81:141–156
29. Alem B, Abedian A, Nasrollahi-Nasab K (2016) Reference-free damage identification in plate-like structures using Lamb-wave propagation with embedded piezoelectric sensors. *J Aerosp Eng* 29(6):04016062
30. Sun H, Zhang A, Wang Y, Qing X (2019) Baseline-free damage imaging for metal and composite plate-type structures based on similar paths. *Int J Distrib Sens Netw* 15(4):1550147719843054
31. Daubechies I (1992) Ten lectures on wavelets. Society for industrial and applied mathematics, Philadelphia
32. Amiri GG, Jalalinia M, Hosseinzadeh AZ, Nasrollahi A (2015) Multiple crack identification in Euler beams by means of B-spline wavelet. *Arch Appl Mech* 85(4):503–515
33. APC (American Piezo Ceramics) International (2002) APC materials. Accessed 17 Oct 2020
34. Motamed PK, Abedian A, Nasiri M (2020) Optimal sensors layout design based on reference-free damage localization with lamb wave propagation. *Struct Control Health Monit* 27(4):e2490
35. Wang T (2014) Finite element modelling and simulation of guided wave propagation in steel structural members. Doctoral dissertation, University of Western Sydney (Australia)
36. Ng CT, Veidt M (2009) A Lamb-wave-based technique for damage detection in composite laminates. *Smart Mater Struct* 18(7):074006
37. He J, Ran Y, Liu B, Yang J, Guan X (2017) A fatigue crack size evaluation method based on lamb wave simulation and limited experimental data. *Sensors* 17(9):2097
38. Alleyne D, Cawley P (1991) A two-dimensional Fourier transform method for the measurement of propagating multimode signals. *J Acoust Soc Am* 89(3):1159–1168
39. Bartoli I, di Scalea FL, Fateh M, Viola E (2005) Modeling guided wave propagation with application to the long-range defect detection in railroad tracks. *NDT E Int* 38(5):325–334
40. Moser F, Jacobs LJ, Qu J (1999) Modeling elastic wave propagation in waveguides with the finite element method. *NDT E Int* 32(4):225–234
41. Gangadharan R, Murthy CRL, Gopalakrishnan S, Bhat MR, Mahapatra DR (2017) Characterization of cracks and delaminations using PWAS AD Lamb wave based time-frequency methods. *Int J Smart Sens Intell Syst* 3:4
42. Hameed MS, Li Z, Zheng K (2020) damage detection method based on continuous wavelet transformation of lamb wave signals. *Appl Sci* 10(23):8610
43. Bagheri A, Li K, Rizzo P (2013) Reference-free damage detection by means of wavelet transform and empirical mode decomposition applied to Lamb waves. *J Intell Mater Syst Struct* 24(2):194–208
44. Bagheri A, Rizzo P, Li K (2017) Ultrasonic imaging algorithm for the health monitoring of pipes. *J Civ Struct Heal Monit* 7(1):99–121
45. Tang Z, Munir N, Lee TG, Yeom YT, Song SJ (2019) Lamb wave flaw classification in Al plates using time reversal and deep neural networks. *J Korean Phys Soc* 75(12):978–984
46. Alem B, Abedian A, Nasrollahi-Nasab K (2021) Impact of sensor geometric dimensions and installation accuracy on the results of instantaneous shm based on wave propagation using wafer active sensors. *J Aerosp Eng* 34(1):04020100

Publisher's Note Springer Nature remains neutral with regard to jurisdictional claims in published maps and institutional affiliations.

Springer Nature or its licensor holds exclusive rights to this article under a publishing agreement with the author(s) or other rightsholder(s); author self-archiving of the accepted manuscript version of this article is solely governed by the terms of such publishing agreement and applicable law.